INORGANIC CHEMISTRY

FRONTIERS

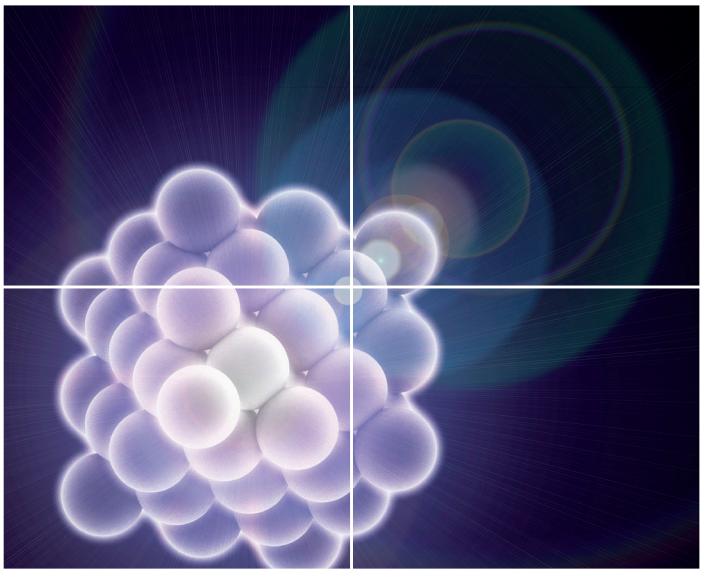

Accepted Manuscript

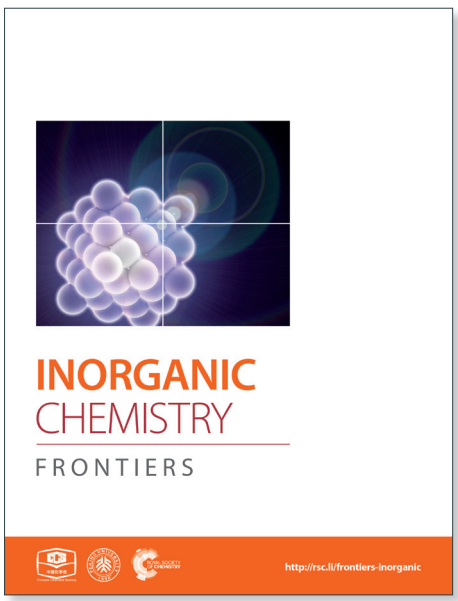

This is an *Accepted Manuscript*, which has been through the Royal Society of Chemistry peer review process and has been accepted for publication.

Accepted Manuscripts are published online shortly after acceptance, before technical editing, formatting and proof reading. Using this free service, authors can make their results available to the community, in citable form, before we publish the edited article. We will replace this *Accepted Manuscript* with the edited and formatted *Advance Article* as soon as it is available.

You can find more information about *Accepted Manuscripts* in the **Information for Authors**.

Please note that technical editing may introduce minor changes to the text and/or graphics, which may alter content. The journal's standard **Terms & Conditions** and the **Ethical guidelines** still apply. In no event shall the Royal Society of Chemistry be held responsible for any errors or omissions in this *Accepted Manuscript* or any consequences arising from the use of any information it contains.

Cite this: DOI: 10.1039/c0xx00000x

www.rsc.org/xxxxxx

ARTICLE TYPE

Facile synthesis of anisotropic single crystalline α-Fe_2O_3 nanoplates and their facet-dependent catalytic performance

Sarish Rehman,[a] Wenglong Yang [a], Fei Liu[a] , Yu Hong [b,*], Ting Wang [b] and Yanglong Hou[a,*]

Received (in XXX, XXX) Xth XXXXXXXXX 20XX, Accepted Xth XXXXXXXXX 20XX

DOI: 10.1039/b000000x

In this work, one step solvothermal method was used to synthesize uniform anisotropic hexagonal and cylindrical hematite nanoplates in the presence of methanol and ethylene di-ammine. The phase and morphology of samples were confirmed by X-ray diffraction (XRD) and electron microscopy. Photocatalytic degradation of the methylene blue (MB) was carried out by two different hematite nanoplates to compare their catalytic performance. Systematic study of different parameters affecting the photodegration of MB was performed. Hexagonal nanoplates exposing (110), (102) and (104) facets exhibit enhanced photocatalytic activity compared to the cylindrical nanoplates which expose only (110) and (102) facets, confirming that high catalytic activity of the hexagonal nanoplates is attributed to exposure of more catalytic active facets.

1 Introduction

Morphology control synthesis of nanomaterials are the focus of research because it has tremendous effect on their magnetic, electrochemical[1], optical[2], and physiochemical[3] properties. Therefore, tuning the morphology is of vital significance in developing new nanomaterials with well-defined crystal facets, excellent reactivity and good stability[4, 5]. Recently, several studies have been reported about the facets dependent physical and chemicals properties of nanomaterials. Among the various properties, catalytic behaviour of nanomaterials strongly depends on the crystal morphology and crystal size[6] , while the crystallographic morphology consecutively can be determined by the exposed and enclosed facets [7]. Significant research has been focused on understanding the facet dependent catalytic property[8, 9] of nanomaterials. For instance, high catalytic activity was observed for Pt nanocubes compared to commercial Pt/C due to exposure of high index facets (211) and (411)[10]. Similarly high catalytic oxidation of propylene has been reported by Cu_2O rhombic dodecahedra exposing (110) crystal facet [11]. In addition, enhanced photocatalytic reduction activity was reported for anatase TiO_2 which predominantly exposed (001) and (101) facets[12].

Although major research studies are devoted to metals and semiconductors, a little work directs towards iron oxide, despite of their environmental friendliness, abundant availability and nontoxicity. Hematite (α-Fe_2O_3) which is most stable iron oxide with various morphologies like sphere[13, 14], rods[15], cubes[16-18], nanoribbons[19], elliptic[20], cantaloupe[21], sea-urchin like [22]flower[23, 24], plates[25], nanodiscs[26], nanorings[27] and polyhedron[28-30] has been explored for several application for example solar cell[31, 32], lithium ion battery[33], water splitting[32, 34], gas sensor[35, 36], drug delivery[37], water treatment[38], magnetic devices[39] and so on. These α-Fe_2O_3 nanostructures exhibits facet dependent interesting properties. Recently, Wei and Sun *et al* synthesized self-assembled single crystalline α-Fe_2O_3 nanoplates by glycerine assisted hydrothermal method for gas sensing property. The obtained α-Fe_2O_3 nanoplates were arranged into columnar one dimensional superstructure (CODS) that stacked perpendicular to (001) facet. The α-Fe_2O_3 nanoplates exhibits higher sensitivity towards toxic gases then self-assembled structure (CODS) due to exposure of highly active (001) facet[40]. Liu *et al* reported Al^{3+} assisted α-Fe_2O_3 nanoplates synthesis by solvothermal method using ammonia as solvent. The obtained α- Fe_2O_3 nanoplates are bound by (001) facet and show ferromagnetic behaviour compared to the bulk α- Fe_2O_3 that are antiferromagnetic at lower temperatures [41]. Cai *et al* recently investigated visible light-induced Rhodamine B (RhB) degradation with H_2O_2 over mesocrystalline hematite nanoplates that was synthesized through hydrolysis of $Fe(acac)_3$ in ethanol by adding a small amount of water. However, they observed that distinct high surface area is mainly responsible for the enhanced photocatalytic properties[42]. Liu and Lv *et al.* reported double adsorption assisted single crystal hexagonal nanorods exposing high index (112) facet. They observed that as-synthesized hexagonal α-Fe_2O_3 nanorods exhibits an excellent electrochemical sensing capability towards H_2O_2 due to high-index facets[43]. Similarly kuang and Xie *et al* synthesized (012) faceted pseudocubes, (113) faceted hexagonal bipyramids and (001) faceted α- Fe_2O_3 nanoplates by surfactant free hydrothermal method. They observed their facets dependent catalytic and gas sensing property and found the α-Fe_2O_3 nanocrystals enclosed with facets of high surface energy (pseudocubes with (012)) exhibit excellent catalytic activity and

[a] *Department of Materials Science and Engineering, College of Engineering Peking University, Beijing, 100871, China. E-mail: hou@pku.edu.cn; Fax: +86 10 62753115*

[b] *College of Environmental Science and Engineering, Beijing Forestry University, Beijing 100083, China yuhong829908@gmail.com*

† Electronic supplementary information (ESI) available: Experimental, characterization methods, TEM images of the intermediate products in the synthesis process, Absorption spectra of the MB degradation

gas-sensing ability[44]. However, despite of these advances, the synthesis of monodisperse α-Fe_2O_3 nanoplates with fine shape control as well as continuous tuning of aspect-ratio still remains a challenge. Thus, it is crucial to develop a rational design for the synthesis of α-Fe_2O_3 nanoplates with well-defined exposed crystal facets which is pivotal to investigate the relationship between morphology and catalytic performance.

Here we report the synthesis of uniform thin anisotropic hexagonal and cylindrical nanoplates by one step solvothermal method. Using iron chloride as precursor in the presence of methanol, ethylene di-ammine and sodium acetate hexagonal nanoplates enclosed by (110), (102) and (104) facets are obtained while in the absence of ethylenediamine cylindrical nanoplates enclosed by (110) and (102) facets are achieved. Further the effect of morphology and exposed facets were investigated on visible light induced degradation of organic dye methylene Blue (MB). Present systematic investigations shows that hexagonal nanoplates possess enhanced photodegration of MB due to exposure of high index (104) facet compared to cylindrical nanoplates.

2 Experimental

2.1 Synthesis of Hexagonal Nanoplates

For the synthesis of hexagonal nanoplates 1 mmol of iron chloride hexa-hydrate was dissolved in 10 mL of methanol and 1 mL ethylene di-ammine under stirring to form a homogeneous solution. When completely dissolved then 0.5 mmol of sodium acetate was added to the mixture. Then the mixture was transferred into a stainless-steel autoclave with a capacity of 25 mL, sealed and heated at 180 ◦C for 12 h. After completion of the reaction autoclave was cooled to room temperature naturally. The resulting product was washed with absolute alcohol and distilled water by centrifugation at 10000 rpm until the supernatant was transparent. The final product was dried at 60◦C in a vacuum oven for 12 h for further characterization.

2.2 Synthesis of Cylindrical Nanoplates

For the synthesis of hexagonal nanoplates 1 mmol of iron chloride hexa-hydrate was dissolved in 10 mL of methanol to form a homogeneous solution. When completely dissolved then 0.5 mmol of sodium acetate was added to the mixture. Then the mixture was transferred into a stainless-steel autoclave with a capacity of 25 mL, sealed and heated at 180◦C for 12 h. After completion of the reaction autoclave was cooled to room temperature naturally. The resulting product was washed with absolute alcohol and distilled water by centrifugation at 10000 rpm until the supernatant was transparent. The final product was dried at 60◦C in a vacuum oven for 12 h for further characterization.

2.3 Characterization

Crystal structure analysis was carried out on a Philips X'Pert Pro diffractometer with Cu Kα radiation (λ=1.5405 ˚A) at V=40 kV and I=150 mA, the scanning speed was 4 ° min^{-1}. For morphological evaluation SEM images were recorded on a Hitachi S4800, transmission electron microscopy (TEM) images, selected area electron diffraction (SAED) pattern and high-resolution TEM (HRTEM) images were captured using FEI Tecnai T20 and F30 operating at an accelerating voltage of 200 kV. Raman spectroscopy measurements were conducted on a Reni Shaw 1000 Raman imaging microscope system using an excitation wavelength of 632.8 nm. Nitrogen adsorption–desorption isotherms were obtained on an ASAP 2010 nitrogen adsorption apparatus. XPS measurements were carried out on an Axis Ultra (Kratos Analytical Ltd.) imaging photoelectron spectrometer. The Brunauer-Emmett-Teller (BET) specific were obtained using the BET equation. The Barret–Joyner–Halender (BJH) method was used to determine the pore size distribution.

2.4 Photocatalytic Evaluation

The photocatalytic activity of the as prepared hematite nanoplates for the degradation of methylene blue (MB) was evaluated by measuring the absorbance of the irradiated solution by UV spectrophotometer. For this purpose 10 mg of catalyst was mixed with MB (50 mL, with a concentration of $2x10^{-5}$ M) in a beaker. Afterwards, the above mix solution was magnetically stirred for 30 min in complete dark to get complete adsorption–desorption equilibrium, followed by the addition of 50 mM of hydrogen peroxide solution (H_2O_2, 30 wt.%). Afterward visible light was allowed to transmit through a cutoff filter of 420 nm and suspension was exposed to a 300 W xenon lamp. During exposure to visible light, the suspension was kept stirring at room temperature using a cooling fan. At different intervals of time bout 4 mL of sample was extracted, centrifuged, and filtered through a membrane (0.22 μm in diameter, Agela Technologies). The dye concentration in the filtrate was evaluated by measuring the absorption intensity at 645 nm.

3 Results and Discussions

3.1 Structure Characterization

The crystal structure of the hematite nanoplates were investigated using XRD. Fig. 1 shows the XRD results of two different type of nanoplates which indicate that all the diffraction peaks match well with the rhombohedral hematite (JCPDS no. 33-0664).The diffraction peaks indicate that products are well crystalline as all the peaks are quite sharp and narrow.

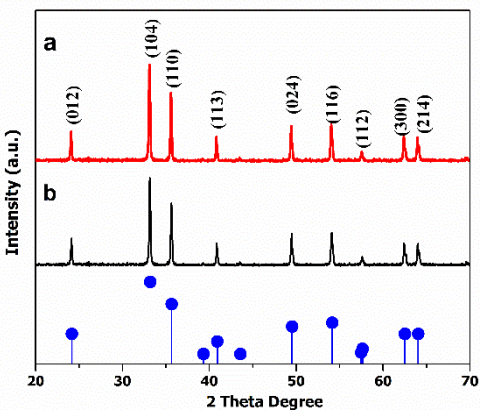

Fig.1 XRD patterns of (a) hexagonal (b) cylindrical nanoplates. The pattern at bottom gives the standard peaks of the α-Fe_2O_3 structure (JCPDS 33-0664).

To determine the anisotropic nature of the hematite nanoplates, crystal facets dependent XRD was performed of the prepared (detail in supporting information (S1)) samples. The peak patterns in the Fig. 2 shows facets dependent XRD for hexagonal nanoplates. It is obvious from the peak intensities (Fig. 2(a)) that (104) facet is dominant in vertically arranged nanoplates while (110) basal facet is the dominant in horizontal one, further TEM studies also confirm these observation as shown in Fig. S1. However, cylindrical nanoplates did not show facet dependent XRD features.

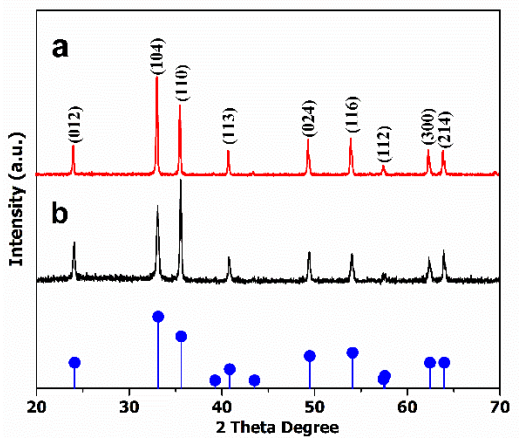

Fig. 2 XRD patterns of anisotropic hexagonal nanoplates standard (a) vertically, (b) horizontally. The pattern at bottom gives the standard peaks of the α-Fe_2O_3 structure (JCPDS 33-0664).

From the SEM image in Fig. 3a it is obvious that product consist of uniform hexagonal nanoplates with narrow size distribution. To further investigate the morphology, TEM characterization was applied. TEM images (Fig. 3b-f) displays highly dispersed hexagonal nanoplates with width of approximately 130-145 nm as confirm by the particle size distribution plot (Fig. S2a). Fig. 3d shows wedge shape edges of the nanoplates with thickness of approximately 3-5 nm (Fig. S2b). High resolution TEM (HRTEM) images (Fig. 3c, e, and f) and selected area diffraction (SAED) patterns shows that products are quite crystalline. HRTEM image in Fig. 3c which has been taken from the white square area of horizontally lying plate shows interplaner distance of about 0.25 nm corresponding to (110) crystal facet of hematite that matches well with XRD results. The SAED pattern in the inset of Fig. 3c shows six equivalents 110 spots which confirm that up and down basal facets of the horizontally lying plates are (110). The HRTEM image taken from the two corners of the vertically lying hexagonal nanoplates clearly shows the lattice spacing of 0.37 nm (Fig. 3e) that can be ascribed to (102) facet on either side. The SEM, SAED pattern and detail investigation of the HRTEM images (Fig. S3a-c) presents terrace –ledge kink (TLK) like surface on edge, where terrace surface corresponds to (102) and ledge structure corresponds to (104) facets. Thus, from TEM, HRTEM and SAED pattern, it can be defined that each hexagonal nanoplates are enclosed by basal (110), smaller (102) and side (104) facets.

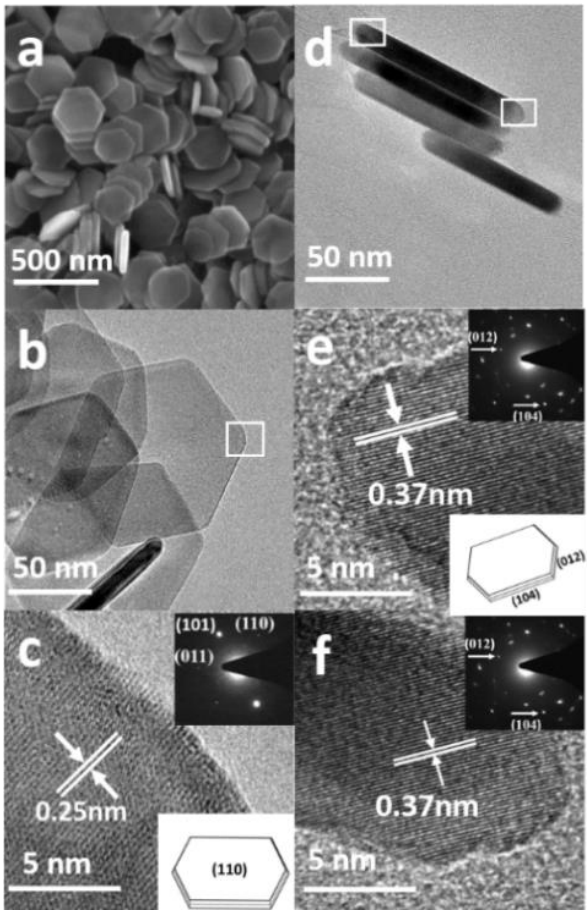

Fig. 3 (a) SEM image (b, c) TEM, HRTEM image, SAED pattern and geometrical model of the hexagonal nanoplates when it lie horizontally (d, e, f) TEM, HRTEM image, SAED pattern and geometrical model of the hexagonal nanoplates when it stands vertically.

The SEM image in Fig. 4a presents the morphology of uniform cylindrical nanoplates with narrow size distribution. High magnification TEM image (Fig. 4c) shows highly dispersed 30-50 nm wide cylindrical shape nanoplates with wedge shape edges as confirm from the particle size distribution plot (Fig. S4). The HRTEM image (Fig. 4d) and SAED pattern in right corner displays clear lattice spacing of 0.25nm and two circle of six equivalent spot that can be ascribed to (110) and (012) facets. Based on the above systematic investigations, characterization (Fig. S5a, b) and schematic geometric model in the inset of Fig. 4b it can be concluded that cylindrical nanoplates are enclosed by (110) basal and smaller (012) facets.

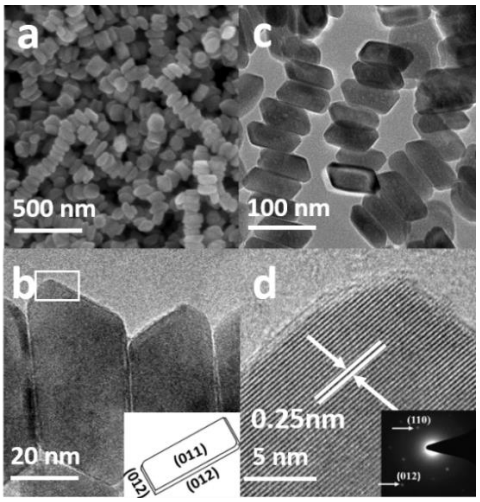

Fig.4 (a) SEM image (b, c, d) TEM, HRTEM images, SAED pattern and geometrical model of the cylindrical nanoplates.

For further confirmation of phase purity, Raman and x-ray photoelectron spectroscopy were used as these are highly sensitive to Fe^{2+} and Fe^{3+} oxidation states[45]. Fig. 5 shows five major characteristic bands that can be assigned to two classes of Raman active vibration modes, *i.e.*, A1g modes (227, 496 cm^{-1}) and Eg modes (293, 411, 615 cm^{-1}), which confirm that both type of nanoplates are α-Fe_2O_3. The XPS spectra (Fig. S6) consist of two peaks one at 710.9 eV and second on 724.8 eV with a satellite peak at 719.2eV that is characteristic of α-Fe_2O_3 phase.

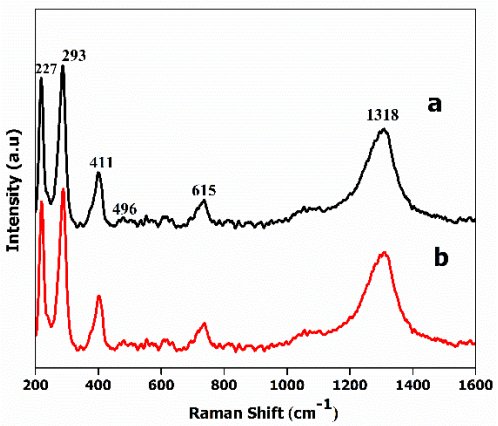

Fig. 5 Raman spectra of (a) hexagonal and (b) cylindrical nanoplates.

3.2 Formation Mechanism of the different Morphology

In this work, ethylene di-ammine played a key role in controlling the morphology of the hematite nanoplates. When ethylene di-ammine and methanol mix solvents were used, then it leads to hexagonal morphology. Ethylene di-ammine acts as chelating agent and also provides basic condition in the presence of sodium acetate for the synthesis of hexagonal nanoplates. Under basic condition, ethylene di-ammine attached (110), (012) and (104) facets uniformly which results in the growth of these facets and leads to the formation of uniform hexagonal nanoplates. While in absence of ethylene di-ammine the growth of (110) and (012) facets take place rapidly as compared to the (104) facet that finally lead to cylindrical nanoplates exposing only two facet compared to hexagonal nanoplates.

Controlled experiments with different time duration were carried out to investigate the detail growth mechanism of the hexagonal and cylindrical nanoplates. Different morphology of the intermediate products synthesize in the presence of ethylene di-ammine are shown in the Fig. S7. As shown in the TEM images (Fig. S7a) when reaction time is 2 h then product consists of small nanoparticles less the 10 nm with spherical morphology. The sample collected after 4 h shows aggregation of the small nanoparticles into large cubic flower like morphology which confirms that small nanoparticles have been gathered to form the building blocks of nanoplates. Increasing the reaction time lead to compact plate like morphology with the existence of small nano particles but still not proper hexagonal in shape. Perfect hexagonal nanoplates were formed after 12 h reaction time, which confirms that 12 h is the minimum time for aggregation of small nanoparticles into complete hexagonal nanoplates with sharp corners. Similarly, cylindrical nanoplates also shows different morphologies at different reaction stage as obvious from TEM images (Fig. S8). The product consists of small nanoparticles of irregular morphology after 3 h reaction time, while the increasing the reaction time leads to cylindrical morphology with attached small nanoparticles (Fig. S8b). Complete cylindrical nanoplates with wedge like edges are obtained after 12 h. The detail investigation of the mechanism reveals that cylindrical nanoplates are formed by the oriented aggregation and Ostwald ripening process of the small nanoparticles. The formation mechanism, aggregation and Ostwald ripening of the hexagonal and cylindrical nanoplates are presented in the scheme 1.

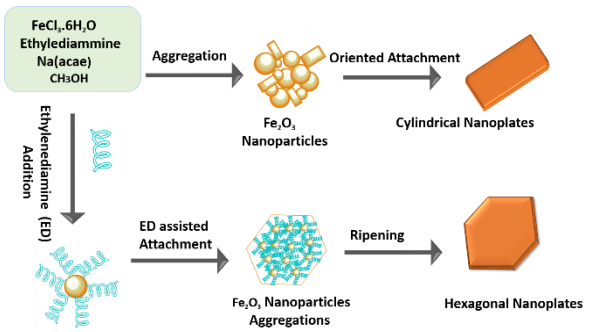

Scheme 1 Schematic illustration of the formation mechanism of hexagonal and cylindrical hematite nanoplates.

3.3 Photocatalytic degradation of organic dye by different architecture of hematite

Methylene blue dye was selected for photocatalytic degradation by two types of hematite nanoplates. Uv-vis spectra of MB degradation in the presence of H_2O_2 additive and visible light at different time intervals are shown in Fig. S9. There is decrease in the absorbance of both the UV and visible regions as well as the shift to lower wavelength of the major peak of absorbance occur with increase in irradiation time. The decrease in the UV-vis spectra with increase of irradiation time occurs due to the degradation of the MB *via* hematite nanoplates. The original absorbance in Fig. S9 shows the adsorption that was measured when the hematite nanoplates were added to dye solution and stirred for 30 min in the dark without H_2O_2 additive. The nitrogen

adsorption isotherm (Fig. S10) reveals that the cylindrical nanoplates have high surface area compared to hexagonal nanoplates but still it exhibits lower catalytic performance. As given in Table 1 the reaction rates are calculated on the base of active sites. The number of active sites in Fe_2O_3 nanoplates can be attribute to the number of Fe^{3+} on different exposed crystal facets. The surface Fe^{3+} play a key role in the generation of ($OH^{\cdot}$) radicals in heterogeneous photo-Fenton reaction *via* redox cycle between Fe^{2+} and Fe^{3+}.So the density of exposed Fe^{3+} are mainly responsible for high catalytic activity[46]. Literature reports shows that the density of exposed Fe^{3+}on (104) facets of hematite is 10.3 atoms nm^{-2} (298.7 atoms/g for hexagonal nanoplates in our case)[18, 29], which is higher than that of (012) facets 7.3 atoms nm^{-2} (212 atoms/g for hexagonal nanoplates) thus indicating (104) facet is more active compared to (102) facet, and should facilitate the MB degradation compared to cylindrical nanoplates which did not expose the (104) facet.

Table 1 Physical properties of the hexagonal and cylindrical nanoplates

Sample	BET Surface area(m^2/g)	Exposed facets	Reaction Rate Constant K(min^{-1})
Hexagonal Nanoplates	29	(110),(012),(104)	0.053
Cylindrical Nanoplates	37	(110),(012)	0.016

So from the detail investigation study of MB degradation by two types of hematite nanoplates, it is concluded that for photocatalytic degradation of organic dyes the surface area does not play an important role. But the exposed crystal facets of the nanomaterials have dominant role in the degradation of the dyes. It is found that hexagonal nanoplates take just 20 min for MB degradation while cylindrical nanoplates requires longer time as shown in Fig. 6.

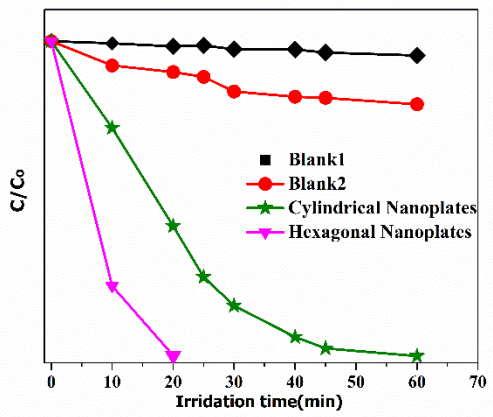

Fig. 6 Photodegradation of MB via two different α-Fe_2O_3 nanoplates under visible-light illumination in the presence of H_2O_2 additive (blank1: photodegradation of MB without additive under visible-light illumination, blank 2: photodegradation of MB under visible-light illumination in the presence of H_2O_2 only).

The catalyst also shows high stability after being used for the photodegradation of MB. The XRD peaks of both the hexagonal and cylindrical nanoplates show (Fig. S11) that no change occurs in the crystal structure after photocatalysis.

3.4 Effect of different parameters on the degradation of MB

In order to study the influence of different parameters on the degradation of MB dye different control experiments were carried out and their affect are discussed below one by one.

3.4.1 Effect of loading of hematite nanoplates

Fig. 7 represents the degradation of MB in the presence of various concentrations of α-Fe_2O_3 nanoplates and H_2O_2 as additive. As shown in the plot (Fig. 7) that after addition of the nanoplates to dye solution significant degradation occurred and after that increasing the catalyst dosage the activity become constant .The reason for this observation is thought that Fe_2O_3 nanoplates act as peroxidase like catalyst for the degradation of MB that cause the generation of ($OH^{\cdot}$) radicals form H_2O_2. But beyond a certain limit no increase in the degradation occurs as there are no dye to be adsorb on the surface of the catalyst. So, we can conclude that 0.6g/L is the maximum amount at which we can get faster degradation of MB dye in shorter duration.

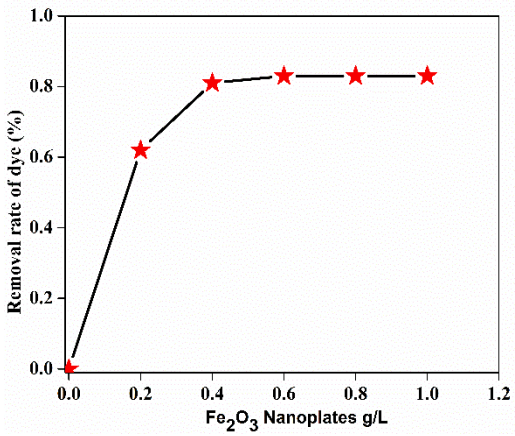

Fig. 7 Effect of hematite nanoplates concentration on the photocatalytic degradation of MB

3.4.2 Effect of pH value of solution

The pH value of the system also has a significant effect on the peroxidase like catalytic degradation of the organic dye. Here, the effect of different pH on the degradation of MB have been studied. It is shown the Fig. 8 that at low pH the degradation is slow, however when the pH value increased to 3 by addition of H_2O_2 a significant enhancement in the degradation occurred because it is difficult for the H_2O_2 to generate the ($OH^{\cdot}$) radicals in weak acidic or basic aqueous solutions, further increasing the pH increase the MB degradation however after pH 4.5 when the pH value has been further increased then degradation efficiency has become slower. So the suitable pH for MB degradation in the presence of α-Fe_2O_3 nanoplates is in the range of 2.5-4.5.

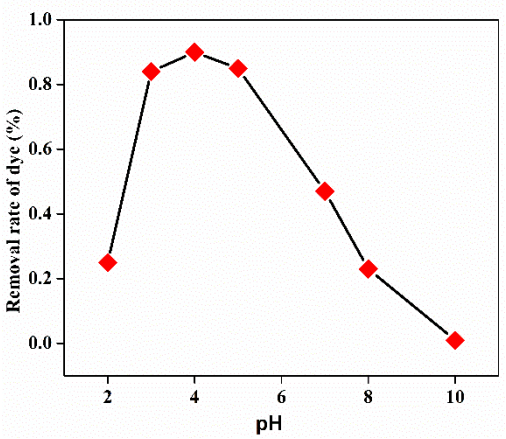

Fig. 8 Effect of pH value on the photocatalytic degradation of MB

3.4.3 Effect of H_2O_2 concentration

H_2O_2 concentrations also affect the degradation efficiency of organic dye, therefore it is explored by using different H_2O_2 concentrations. In the catalytic degradation of MB H_2O_2 is mainly responsible to generate ($OH^{\cdot}$) radicals, so increasing the H_2O_2 concentration the degradation efficiency of MB increase but further increase in the concentration has no effect on the degradation due to the limited amount of the catalyst. As shown in the Fig. S5 (a) that in the absence of H_2O_2 hematite nanoplates are not able to do the degradation of MB. Fig. 9 shows that optimal concentration (0.25-0.65 mmol/L) of H_2O_2 is required for faster degradation of MB in shorter time.

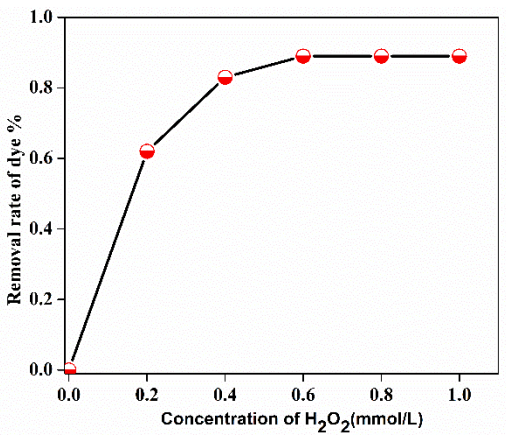

Fig. 9 Effect of H_2O_2 concentration on the photocatalytic degradation of MB

The mechanism of the MB degradation by hematite is explain schematically (scheme 2).When the dye is exposed to visible light then it is excited and in this state it is adsorbed on the surface of nanoplates where electron transfer occur from the excited dye and generate Fe^{2+} to oxidize the dye. The Fe^{2+} is mainly responsible for the generation of OH radical from H_2O_2 and degradation of MB takes place by hydrophilic attack of OH radical on the C-N bond and replaces it by aryl bond. The C-N bond is the main chromophoric agent in the MB dye. Afterward subsequent degradation of the MB takes place via hematite nanoplates.

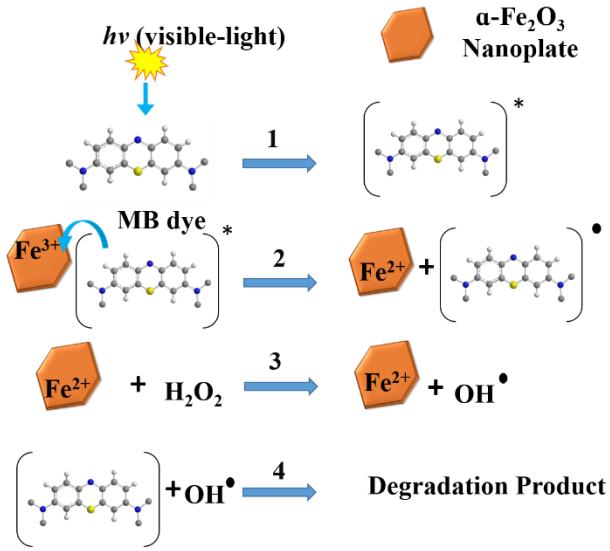

Scheme 2 Illustration of the MB degradation by hematite nanoplates

4 Conclusion

In summary, a facile one step solvothermal method was used to synthesize two kind of uniform thin anisotropic hexagonal nanoplates exposing (110), (102) and (104) facets and cylindrical nanoplates enclosed by (110) and (102) facets in the presence of methanol, ethylene di-ammine and sodium acetate. To explore the photocatalytic activity of as-synthesized different types of nanoplates degradation of MB was carried out. The enhanced photocatalytic performance of hexagonal nanoplates is attributed to the exposure of high-index facets. It is expected that highly active, stable, cost effective and potential catalyst can be applied for the photodegradation of the organic dyes.

Acknowledgements

This work was supported by the NSFC (51125001, 51172005), Beijing Natural Science Foundation (2122022), NSFC-RGC Joint Research Scheme (51361165201), Doctoral Program of the Ministry of Education of China (20120001110078), the Interdisciplinary Project of Beijing New Star Plan of Science and Technology. We thank Kishwar Khan for the kind discussion.

Notes and References

1. J. Ma, J. Lian, X. Duan, X. Liu and W. Zheng, *The Journal of Physical Chemistry C*, 2010, **114**, 10671-10676.
2. D. K. Bora, A. Braun, R. Erni, G. Fortunato, T. Graule and E. C. Constable, *Chemistry of materials*, 2011, **23**, 2051-2061.
3. X. Liu, D. Wang and Y. Li, *Nano Today*, 2012, **7**, 448-466.
4. X. Mou, X. Wei, Y. Li and W. Shen, *CrystEngComm*, 2012, **14**, 5107-5120.
5. X. Xie and W. Shen, *Nanoscale*, 2009, **1**, 50-60.
6. Y. Li and W. Shen, *Science China Chemistry*, 2012, **55**, 2485-2496.
7. M. H. Huang and P. H. Lin, *Advanced Functional Materials*, 2012, **22**, 14-24.
8. Y. Li and W. Shen, *Chemical Society Reviews*, 2014, **43**, 1543-1574.

9. Y. Li and W. Shen, *Nanocatalysis: Synthesis and Applications*, 2013, 333.
10. L. Zhang, D. Chen, Z. Jiang, J. Zhang, S. Xie, Q. Kuang, Z. Xie and L. Zheng, *Nano Research*, 2012, **5**, 181-189.
11. Q. Hua, T. Cao, X. K. Gu, J. Lu, Z. Jiang, X. Pan, L. Luo, W. X. Li and W. Huang, *Angewandte Chemie*, 2014, **126**, 4956-4961.
12. J. Yu, J. Low, W. Xiao, P. Zhou and M. Jaroniec, *Journal of the American Chemical Society*, 2014, **136**, 8839-8842.
13. G. Liu, Q. Deng, H. Wang, D. H. Ng, M. Kong, W. Cai and G. Wang, *Journal of Materials Chemistry*, 2012, **22**, 9704-9713.
14. T. Yang, Z. Huang, Y. Liu, M. Fang, X. Ouyang and M. Hu, *Ceramics International*, 2014.
15. J. Yeo, S. Hong, W. Manorotkul, Y. D. Suh, J. Lee, J. Kwon and S. H. Ko, *The Journal of Physical Chemistry C*, 2014, **118**, 15448-15454.
16. H. Liang, X. Jiang, Z. Qi, W. Chen, Z. Wu, B. Xu, Z. Wang, J. Mi and Q. Li, *Nanoscale*, 2014.
17. W. Qin, C. Yang, R. Yi and G. Gao, *Journal of Nanomaterials*, 2011, **2011**, 3.
18. W. Wu, R. Hao, F. Liu, X. Su and Y. Hou, *Journal of Materials Chemistry A*, 2013, **1**, 6888-6894.
19. R. Xu, H. Yan, W. He, Y. Su, J.-C. Nie and L. He, *The Journal of Physical Chemistry C*, 2012, **116**, 6879-6883.
20. Z. An, J. Zhang, S. Pan and F. Yu, *The Journal of Physical Chemistry C*, 2009, **113**, 8092-8096.
21. L.-P. Zhu, H.-M. Xiao and S.-Y. Fu, *Crystal Growth & Design*, 2007, **7**, 177-182.
22. X. Liu, Z. Chang, L. Luo, X. Lei, J. Liu and X. Sun, *Journal of Materials Chemistry*, 2012, **22**, 7232-7238.
23. X. Zhou, G. Zhao and Y. Liu, *Materials Letters*, 2013, **95**, 33-36.
24. Y. Han, Y. Wang, L. Li, Y. Wang, L. Jiao, H. Yuan and S. Liu, *Electrochimica Acta*, 2011, **56**, 3175-3181.
25. Y. Ni, X. Ge, Z. Zhang and Q. Ye, *Chemistry of materials*, 2002, **14**, 1048-1052.
26. J. S. Chen, T. Zhu, X. H. Yang, H. G. Yang and X. W. Lou, *Journal of the American Chemical Society*, 2010, **132**, 13162-13164.
27. X. Hu, J. C. Yu, J. Gong, Q. Li and G. Li, *Advanced Materials*, 2007, **19**, 2324-2329.
28. S. Li, G. Qin, X. Meng, Y. Ren and L. Zuo, *Journal of Materials Science*, 2013, **48**, 5744-5749.
29. B. Lv, Z. Liu, H. Tian, Y. Xu, D. Wu and Y. Sun, *Advanced Functional Materials*, 2010, **20**, 3987-3996.
30. H.-J. Song, X.-H. Jia and X.-Q. Zhang, *Journal of Materials Chemistry*, 2012, **22**, 22699-22705.
31. Y. Lin, S. Zhou, S. W. Sheehan and D. Wang, *Journal of the American Chemical Society*, 2011, **133**, 2398-2401.
32. G. Wang, Y. Ling, D. A. Wheeler, K. E. George, K. Horsley, C. Heske, J. Z. Zhang and Y. Li, *Nano letters*, 2011, **11**, 3503-3509.
33. X. Zhu, Y. Zhu, S. Murali, M. D. Stoller and R. S. Ruoff, *ACS Nano*, 2011, **5**, 3333-3338.
34. Y. Ling, G. Wang, D. A. Wheeler, J. Z. Zhang and Y. Li, *Nano letters*, 2011, **11**, 2119-2125.
35. J. Ma, L. Mei, Y. Chen, Q. Li, T. Wang, Z. Xu, X. Duan and W. Zheng, *Nanoscale*, 2013, **5**, 895-898.
36. P. K. Kannan and R. Saraswathi, *Journal of Materials Chemistry A*, 2014, **2**, 394-401.
37. M. Colombo, S. Carregal-Romero, M. F. Casula, L. Gutiérrez, M. P. Morales, I. B. Böhm, J. T. Heverhagen, D. Prosperi and W. J. Parak, *Chemical Society Reviews*, 2012, **41**, 4306-4334.
38. L. S. Zhong, J. S. Hu, H. P. Liang, A. M. Cao, W. G. Song and L. J. Wan, *Advanced Materials*, 2006, **18**, 2426-2431.
39. H. Zeng, J. Li, J. P. Liu, Z. L. Wang and S. Sun, *Nature*, 2002, **420**, 395-398.
40. X.-W. Wei, J. Sun, K.-L. Wu, X.-Z. Li, C. Dong, X.-W. Wang, B. Zhang, Z.-X. Zhang and J. Huang, *CrystEngComm*, 2014.
41. R. Liu, Y. Jiang, Q. Lu, W. Du and F. Gao, *CrystEngComm*, 2013, **15**, 443-446.
42. J. Cai, S. Chen, M. Ji, J. Hu, Y. Ma and L. Qi, *CrystEngComm*, 2014, **16**, 1553-1559.
43. Z. Liu, B. Lv, Y. Xu and D. Wu, *Journal of Materials Chemistry A*, 2013, **1**, 3040-3046.
44. J. Ouyang, J. Pei, Q. Kuang, Z. Xie and L. Zheng, *ACS applied materials & interfaces*, 2014, **6**, 12505-12514.
45. Y. Zeng, R. Hao, B. Xing, Y. Hou and Z. Xu, *Chem. Commun.*, 2010, **46**, 3920-3922.
46. W. Du, Q. Sun, X. Lv and Y. Xu, *Catalysis Communications*, 2009, **10**, 1854-1858.

TOC

Facet dependent Photocatalytic degradation of Methylene Blue was carried out by hexagonal and cylindrical hematite nanoplates.